

SOFIA/FORCAST Monitoring of the Dust Emission from R Aqr: Start of the Eclipse

RAVI SANKRIT ¹, ERIC OMELIAN ², UMA GORTI ^{3,4}, R. MARK WAGNER ⁵,
STEVEN GOLDMAN ¹ AND PATRICIA A. WHITELOCK ^{6,7}

¹*Space Telescope Science Institute, 3700 San Martin Drive, Baltimore, MD 21218, USA*

²*Space Science Institute, 4765 Walnut St., Suite B, Boulder, CO 80301, USA*

³*Carl Sagan Center, SETI Institute, Mountain View, CA 94043, USA*

⁴*NASA Ames Research Center, Moffett Field, CA 94035, USA*

⁵*The Ohio State University, LBT Observatory, 933 N. Cherry Ave, Tucson, AZ 85721, USA*

⁶*South African Astronomical Observatory, P.O. Box 9, Observatory, 7935 Observatory, South Africa*

⁷*Department of Astronomy, University of Cape Town, Private Bag X3, Rondebosch 7701, South Africa*

(Received; Revised; Accepted 22-Dec-2021)

Submitted to ApJ

ABSTRACT

We present mid-infrared spectra from our continued monitoring of R Aquarii, the nearest symbiotic Mira, using the Stratospheric Observatory for Infrared Astronomy (SOFIA). New photometric and spectroscopic data were obtained with the Faint Object infraRed CAmera for the SOFIA Telescope (FORCAST) in 2018 and 2019 after the system had started its “eclipse”, during which it became two magnitudes fainter in the visual. The mid-IR flux, in particular the $10\mu\text{m}$ silicate feature, have strengthened compared with the previous cycles. Radiative transfer models for the circumstellar dust emission were calculated for the new spectra, and re-calculated for those previously obtained using more appropriate values of the near-IR magnitudes to constrain the properties of the AGB spectra heating the dust. The modeling shows that the luminosity dependence on pulsation phase is not affected by the onset of the eclipse, and that the increase in the mid-IR flux is due to a higher dust density. The models also confirm our earlier results that micron-size grains are present, and that no changes in the grain composition are required to explain the variations in the spectra.

Corresponding author: Ravi Sankrit
rsankrit@stsci.edu

Keywords: Asymptotic giant branch (108); Symbiotic binary stars (1674); Circumstellar dust (236); Stellar pulsations (1625)

1. INTRODUCTION

R Aquarii (R Aqr), at a distance of 218 pc (Min et al. 2014) is the closest symbiotic system. It consists of an M-type Mira variable with a steady pulsation period of 387 days (Belczyński et al. 2000), and a hot compact companion, which has a temperature of about 60,000 K, and a luminosity in the range 5–20 L_{\odot} (Kaler 1981; Burgarella et al. 1992). The hot star is either a White Dwarf (WD) or a subdwarf on the evolutionary track toward a WD state (Burgarella et al. 1992). Henceforth we will use the term WD for the hot component of the binary. The WD sustains a compact ionized nebula (Meier & Kafatos 1995) beyond which lie complex nebular structures extending several arcminutes away from the central binary, which are probably due to nova-like ejections of material many centuries ago (Solf & Ulrich 1985; Liimets et al. 2018). The system also contains a spectacular jet (e.g. Melnikov et al. 2018) that is most likely driven by the accretion flow of material from the cool Asymptotic Giant Branch (AGB) star onto the WD. R Aqr is a “Dusty”, or D-type symbiotic, because it is a bright infra-red (IR) source. It is also known as a symbiotic Mira (Whitelock 1987), although it is rather less dusty than is typical for this class. The IR emission is dominated by the circumstellar shell, and the spectral energy distribution (SED) consists of the stellar blackbody plus a thermal dust component. An early spectrum (Merrill & Stein 1976) revealed the presence of the prominent 9.7 μm silicate feature, known to be characteristic of M-type AGB stars (Woolf 1973).

Based on successive periods of visual dimming of R Aqr during 1928–1934 and 1974–1980, Willson et al. (1981) inferred an orbital period of about 44 years, and suggested that the decrease in brightness was due to a dusty accretion stream obscuring the Mira. Gromadzki & Mikołajewska (2009a) refined the period to 43.6 years, and showed that the dimming occurs as the WD eclipses its Mira companion, and that the periastron passages occur during these times. The current eclipse has started (§2.2, Fig. 1; note that henceforth we will use the term “eclipse” to refer generally to this period of visual dimming), and the periastron will occur in 2023.

We initiated a program in 2016 to monitor R Aqr at mid-IR wavelengths using the Stratospheric Observatory for Infrared Astronomy (SOFIA). In Omelian et al. (2020) (Paper 1) we presented observations using SOFIA/FORCAST in 2016, and 2017, supplemented with observations using the Infrared Space Observatory (ISO) obtained in 1996, when the system was near apastron. We modeled the mid-IR SED at these epochs and, based on the strengths of the silicate features, showed that there had been a significant decrease in the dust density between apastron and the current epoch. The models also showed that the change in the SED between 2016 and 2017 did not require any modifications to the composition of the emitting grains,

but instead could be explained by variations with pulsation-phase of the effective temperature of the AGB star, the inner radius of the dust shell, and the dust density at this inner radius.

In this paper we present the SOFIA/FORCAST observations of R Aqr obtained during Cycle 6 (2018) and Cycle 7 (2019), and follow the evolution of the mid-IR SED. The new data are modeled using the method described in Paper 1. We also calculate revised models for the ISO, and SOFIA Cycles 4 and 5 data using updated values for the near-IR (*JHKL*) fluxes.

The observations are presented in §2, and the FORCAST flux measurements in §3. In §4 the modeling procedure is outlined, and the need for updated models for the earlier data is explained. The results and their implications are discussed in §5, and §6 contains some concluding remarks.

2. OBSERVATIONS

As part of our continued monitoring of R Aqr in the mid-IR, we obtained photometric and spectroscopic data using FORCAST on board SOFIA (Young et al. 2012) on August 24, 2018 and October 16, 2019 (all dates are UTC) during Observing Cycles 6 and 7, respectively. The FORCAST instrument (Herter et al. 2013) has a suite of imaging filters and low-dispersion grisms, and covers the 5.4–37.5 μm wavelength region, except for a gap between about 13.5 and 17.5 μm . Although this gap wavelength region has been accessed on airborne observatories (e.g. Forrest et al. 1979), the strong molecular absorption bands reduce the transmission close to zero even in the stratosphere.

These new observations were obtained using the same strategy as in Cycles 4 and 5 (Paper 1). All the standard photometric filters between 6.4 μm and 37.5 μm were used in dual-channel mode. Although the overall wavelength coverage remains the same, the set of filters is not identical from cycle-to-cycle. Spectroscopic observations were obtained using the G111 (8.4–13.7 μm) and G227 (17.6–27.7 μm) grisms in both cycles. Additionally, in Cycle 7, spectra were obtained using the G329 (28.7–37.1 μm) grism. All spectra were taken through the 4.7'' slit yielding spectral resolutions, $R = 130, 110$ and 160 for the G111, G227, and G329 data, respectively. The data were obtained using standard chopping and nodding, along with 3-point dithers to remove the effects of bad pixels. The exposure times were dominated by overhead, with on-source times of approximately 30 to 60 seconds for each setting.

For this study, we used the flux-calibrated “Level 3” data products that are provided by the SOFIA Science Center. The flux calibration factors are obtained from observations of standard stars, except in the case of G227 and G329 spectra, which use bright asteroids. The details are available in the “Guest Observer Handbook for FORCAST Data Products” provided by SOFIA, and available on their website. The wavelength coverage of the G111 grism includes the ozone feature at 9.6 μm over which the calibration is unreliable, and therefore we exclude the spectral data between

9.2 and 10.3 μm in our analyses. The long-wavelength end of the G329 spectrum is poorly calibrated due to a strong terrestrial feature, and therefore we exclude the data longward of 35 μm .

Table 1. Mid-IR Observations of R Aqr

Observation	Obs. Date	V ^a	ϕ_{Mira} ^b
ISO	1996 May 16	8.0	0.14
SFC4 ^c	2016 Sep 22	10.6	0.35
SFC5	2017 Aug 7	8.5	0.17
SFC6	2018 Aug 24	9.4	0.16
SFC7	2019 Oct 16	11.5	0.24

^aVisual magnitude from AAVSO

^b $\phi_{Mira} = 0.0$ (visual maximum) on 2005 October 6, period = 387.0 days

^cSOFIA Cycle 4, et. seq.

Table 1 lists the mid-IR observations, the dates they were obtained, and the visual magnitude and Mira phase on the observation date. Figure 1 shows the light curve for R Aqr from December 2014 through September 2021. The system was about two magnitudes fainter in the visual at the three most recent pulsation maxima (2019 mid-June, 2020 early-July, and 2021 late-July) compared with previous cycles, indicating that the eclipse has started. The Cycle 4 and 5 SOFIA/FORCAST observations were obtained before the onset of the eclipse, and Cycle 7 observations after it started (Fig. 1). The Cycles 5 and 6 observations were obtained at approximately the same Mira pulsation phase, but the system was about one magnitude fainter on the latter date than on the former (Table 1). This suggests that the dimming had started before the Cycle 6 observations were obtained.

2.1. Historical JHKL Data

R Aqr was monitored at near-IR wavelengths between 1980 and 2014 using the MkII photometer on the 0.75m telescope at the Sutherland site of the South African Astronomical Observatory. The early data were published and/or discussed by Catchpole et al. (1979); Whitelock et al. (1983); Whitelock (1987); Gromadzki et al. (2009b), but the entire data-set is presented in Table A1 as the monitoring program was terminated in 2014. These data are on the photometric system described by Carter (1990), which can be converted to the 2MASS system following Carpenter (2001). This involved some very small (< 0.05 mag) corrections to the data published prior to 1990. The photometry is accurate to better than ± 0.03 in the *JHK* bands, and ± 0.05 in the *L* band.

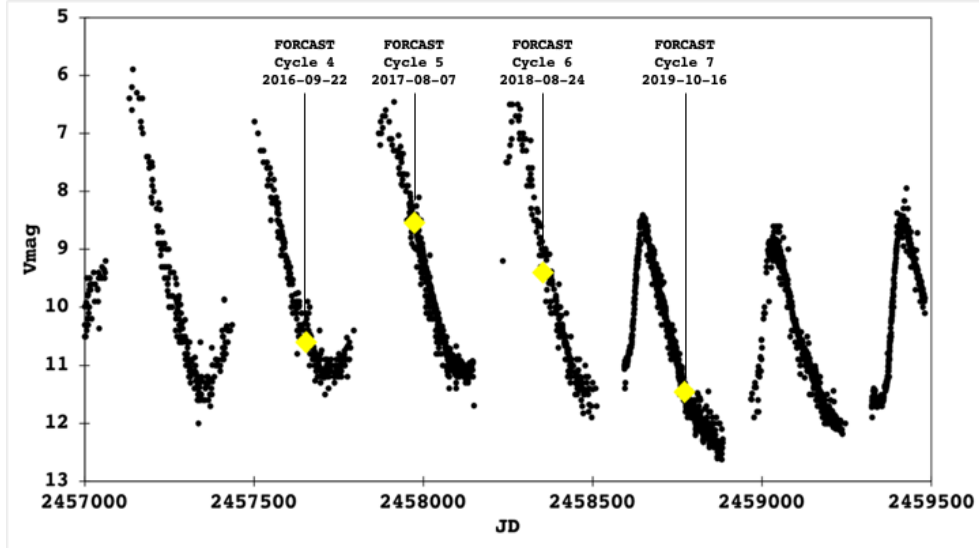


Figure 1. The AAVSO light curve of R Aqr from December 2014 through September 2021. Yellow diamonds indicate the SOFIA FORCAST observations to date.

We use these data to select the best representative values for the dates of the FORCAST observations based on the Mira pulsation phase and visual magnitude. This is discussed further in §4.

3. RESULTS: THE MID-IR SPECTRUM OF R AQR

As in the previous data, the photometric images obtained in Cycles 6 and 7 show that at these wavelengths, R Aqr is consistent with a point source at the FORCAST angular resolution, which ranges from just under $3''$ at $5.4\ \mu\text{m}$ to about $5''$ at $37\ \mu\text{m}$. The mid-infrared emission is thus dominated by the cool AGB star, its accompanying circumstellar dust shell, and possibly the accretion flow. There is negligible contribution from the surrounding nebula, which is prominent at optical wavelengths (e.g. [Liimets et al. 2018](#)).

The fluxes were extracted from the images using aperture photometry as in Paper 1, following the SOFIA FORCAST Photometry Cookbook (version of 4 Sep 2018, Rev A). The source flux is extracted from a 12 pixel radius circular aperture, centered on the flux-weighted centroid of the target. The source radius of 12 pixels corresponds to $9.216''$. The background is defined by an annulus between radii of 15 and 25 pixels centered at the same point as the target. Since the data are already sky-subtracted by the pipeline, the background is used only to establish the photometric uncertainty. In all the images, the median fluxes in the background regions were identically zero, and the standard deviations ranged between 0.01 and 0.03 Jy. The source is sufficiently bright and the photometric uncertainties, η_m , range from 0.05% to 0.63%. The uncertainties in the flux are dominated by the relative error in flux calibration, η_{flux} , obtained from the FITS header values, CALFCTR and ERRCALF, for each observation. These uncertainties range from 1.89 to 2.88% in the SOFIA Cycle 6 data, and 0.90 to 6.10% in the SOFIA Cycle 7 data. The Cookbook lists a

third source of uncertainty, $\eta_{\text{model}} \approx 0.05$, due to the flux calibration model. Since our data in each epoch were obtained on the same flight-legs, the relative uncertainty from the model should be significantly lower, and therefore we do not include this term in our error calculation. However, we assume that the minimum combined uncertainty for each measurement is 5%.

Table 2. R Aqr: SOFIA FORCAST Photometry

Filter	λ_{eff} (μm)	$\Delta\lambda$ (μm)	Flux SFC4 (Jy)	Flux SFC5 (Jy)	Flux SFC6 (Jy)	Flux SFC7 (Jy)
F056	5.6	0.08	...	1583 (± 380)
F064	6.4	0.14	747 (± 37)	1149 (± 58)	1248 (± 62)	974 (± 49)
F077	7.7	0.47	580 (± 29)	835 (± 42)	963 (± 48)	828 (± 43)
F088	8.8	0.41	1028 (± 51)	...
F111	11.1	0.95	661 (± 79)	883 (± 44)	1024 (± 51)	851 (± 52)
F197	19.7	5.5	359 (± 18)	435 (± 22)	...	441 (± 22)
F253	25.3	1.86	203 (± 16)	254 (± 13)	275 (± 14)	251 (± 13)
F315	31.5	5.7	143 (± 7)	195 (± 14)	204 (± 10)	180 (± 9)
F336	33.6	1.9	131 (± 17)	163 (± 8)	181 (± 9)	161 (± 8)
F348	34.8	3.8	110 (± 6)	139 (± 15)	147 (± 7)	148 (± 7)
F371	37.1	3.3	92 (± 6)	121 (± 7)	129 (± 7)	116 (± 6)

The grism data are subject to slit-losses that are variable, which adds uncertainty to the absolute flux calibration since these losses may be different for the science target and calibrator. Therefore, we scale the spectra to photometric points, using the 11.1 μm flux for the G111 spectra, and the 19.7 μm flux for the G227 spectra. The 19.7 μm data were not obtained during Cycle 6, and the G227 spectrum was scaled instead to the 25.3 μm photometric flux. Scaling the G111 spectra by convolving with the throughput curve of the SOFIA FORCAST 11.1 μm filter yields a difference of less than 0.5%. The G227 grism bandpass does not completely overlap the SOFIA FORCAST 19.7 μm filter throughput. However the spectrum is relatively smooth in that wavelength region, and we expect the difference between the scaling at one wavelength point and convolving with the filter throughput would yield a negligible difference as for the shorter wavelength filter. The G329 grism (28.7-37.1 μm) is also scaled to a photometric point at 33.6 μm by convolving the G329 spectrum with the throughput filter of the 33.6 μm filter. The relative errors in the spectral fluxes for a single spectrum (outside the region affected by ozone for G111 data) are approximately 2%, as determined from the median of the error arrays.

Table 2 lists the filter names, central wavelengths and bandpasses, and measured fluxes and errors for the imaging data from all observing cycles. Figure 2 shows plots of the photometric points and the grism spectra, and also includes the ISO-

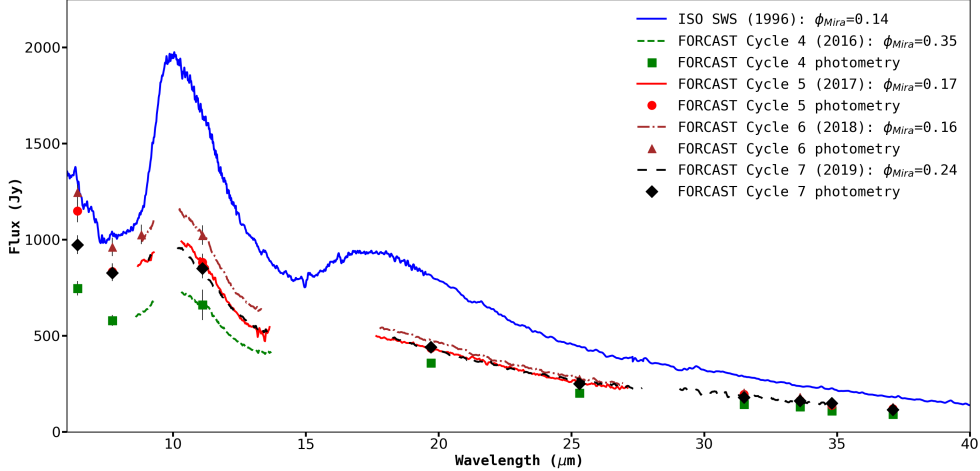


Figure 2. Infrared Spectral Energy Distribution (SED) of R Aqr obtained with ISO, and with SOFIA FORCAST. The spectra around $10 \mu\text{m}$ for the SOFIA FORCAST grism data has been removed due to the telluric atmospheric ozone feature that occurs around this wavelength. The error-bars on the photometric measurements are shown, and are mostly smaller than the symbol size.

SWS spectrum obtained in 1996. The classic silicate spectral features around $10 \mu\text{m}$ and $18 \mu\text{m}$ are evident in the spectral energy distributions at each epoch.

4. RADIATIVE TRANSFER MODELS OF THE DUST EMISSION

In an oxygen-rich AGB star, silicate grains responsible for the $10 \mu\text{m}$ and $18 \mu\text{m}$ features condense in a region of the circumstellar shell just beyond the molecular layer, typically at a distance of about 5–10 stellar radii from the center (e.g. [Gobrecht et al. 2016](#)). The silicate features exhibit a wide range of shapes and relative strengths ([Speck et al. 2000](#); [Kraemer et al. 2002](#)), which depend on the density and temperature of the dust, and on the composition of the grains and their size distribution.

We model the emission from the dust shell using the publicly available three-dimensional radiative transfer code, RADMC-3D ([Dullemond et al. 2012](#)), using the same procedure as in Paper 1. Briefly, the AGB star is placed at the center of the grid, and the dust shell is spherically symmetric around the star, extending between an inner radius R_{in} and an outer radius $R_{out} = 10,000 \text{ au}$. The radial dust density profile is assumed to be $\rho_{dust}(r) = \rho_{in}(r/R_{in})^{-2}$, and is specified at 100 logarithmically spaced intervals in r .

The optical constants used are those for oxygen-deficient circumstellar silicate dust from [Ossenkopf et al. \(1992\)](#), which have bulk density $\rho_{grain} = 3.0 \text{ g cm}^{-3}$. The grain size distribution is the standard [Mathis et al. \(1977\)](#) MRN power-law $n(a) \propto a^{-3.5}$ with $0.001 \mu\text{m} \leq a \leq a_{max}$. In Paper 1 we showed that micron size grains were required to fit the width of the silicate feature, and found that the best fits were obtained with $a_{max} = 3 \mu\text{m}$. The presence of large grains has been described in detail in §5.3 of that paper. We therefore fix a_{max} to be $3 \mu\text{m}$ in all the new model calculations. Spherical grains, and Mie scattering are assumed in the models.

The inner radius (R_{in}) and the dust density at the inner radius (ρ_{in}) are treated as variable input parameters. We include a WD, with $R_{WD}=3 R_{\oplus}$ and $T_{WD}=60,000$ K in the spatial grid, placed at an appropriate distance from the AGB star based on the orbital elements of Gromadzki & Mikołajewska (2009a) for each observation date. The presence of the WD has a local effect, increasing the dust temperature by about 200 K in a region less than about 1 au, but does not impact the overall mid-IR SED, and is included nonetheless for consistency. For the AGB star, its effective temperature, T_{eff} and luminosity are the required input parameters. We use T_{eff} and the stellar radius, R_{\star} and use the Stefan-Boltzmann law to calculate the luminosity.

The best-fit model parameters for each observation are obtained in three stages. In the first stage, the values for the stellar effective temperature and radius were determined using dust-free blackbody models and matching inferred near-IR ($JHKL$) fluxes and the observed 6.4 and 7.7 μm fluxes. Measurements of these parameters using interferometric observations of R Aqr (Danchi et al. 1994; van Belle et al. 1996; Wittkowski et al. 2016) provide us with the range of values for each that we use in the models. T_{eff} was constrained to lie in the range 1800–3000 K, and sampled in steps of 100 K. And R_{\star} was sampled in steps of 0.05 au between 1.6 and 3.0 au.

The $JHKL$ magnitudes appropriate for the observations were obtained from the historical SAAO data, choosing dates when both the Mira-phase and V-magnitude were as close as possible to the values during the mid-IR observations. The ISO observation occurred during the SAAO campaign, and for that we interpolate the magnitudes from the nearest observations, before and after. For SOFIA Cycles 6 and 7, we chose SAAO dates for which the Mira-phase matched the SOFIA observations, but the V-magnitudes were adjusted to match the out-of-eclipse values. The SAAO observation dates, V-magnitudes, Mira-phases, and $JHKL$ magnitudes on those dates are listed in Table 3, and the AGB properties, T_{eff} and R_{\star} , in Table 4,

For the Cycle 6 and 7 data we also ran models using $JHKL$ values from SAAO observations obtained at times when the V-magnitudes were the same as during the SOFIA observations, and phases as close as possible. The dates of these observations were Oct-04-1983 for Cycle 6 when the IR brightnesses were about 0.3 magnitude fainter and January-13-1984 for Cycle 7, when they were about 1.0 magnitude fainter. The models predicted significantly lower AGB luminosities – $6100 L_{\odot}$ and $3400 L_{\odot}$ – and predicted only about 2/3 the observed 6.4 μm and 7.7 μm fluxes.

In the second stage, the AGB properties (T_{eff} and R_{\star}) found in the first stage were used (Table 4). Models were calculated for each observation with inner radius values of 10, 15, 20 and 25 au, with dust added in each case to match the observed 11.1 μm flux. As in Paper 1, we started with ρ_{in} equal to 10^{-19} g cm^{-3} , based on the mass loss rates from Danchi et al. (1994), and adjusted this value until visual inspection of plots with model spectra overlaid on the data showed a good match. The initial values of ρ_{in} lay in the range $3\text{--}35 \times 10^{-20}$ g cm^{-3} .

Table 3. SAAO Observation Dates, and JHKL Photometry

Observation	SAAO Obs.	V ^a	ϕ_{Mira} ^b	<i>J</i>	<i>H</i>	<i>K</i>	<i>L</i>
ISO	interpolated	8.0 ^c	0.14 ^c	0.05	-0.97	-1.47	-2.13
SFC4	2001 Nov 27	10.7	0.36	0.62	-0.48	-1.04	-1.62
SFC5	1987 Dec 14	8.5	0.19	-0.06	-1.05	-1.52	-2.18
SFC6	1987 Dec 14	8.5	0.19	-0.06	-1.05	-1.52	-2.18
SFC7	1985 Nov 21	9.5	0.24	0.18	-0.87	-1.40	-2.04

^aVisual magnitude from AAVSO

^b $\phi_{Mira} = 0.0$ (visual maximum) on 2005 October 6, period = 387.0 days

^cInterpolated to the date of the ISO observation, therefore identical to the values in Table 1

Table 4. Model Input Parameters for AGB Star Properties

Model	R_{\star} (au)	T_{eff} (K)	L_{\star}/L_{\odot}
ISO	2.35	2500	9000
SFC4	2.30	2200	5200
SFC5	2.55	2400	9000
SFC6	2.55	2400	9000
SFC7	2.40	2400	8000

In the third and final stage of the modeling, the stellar temperatures and radii were held fixed for each observation. Then, a set of models were calculated for each of $R_{in} = 10, 15, 20$ and 25 au, in each case varying ρ_{in} in steps of 0.25×10^{-20} g cm⁻³ around the value found in the second stage. The Pearson χ^2 statistic was calculated on the difference between the model and the data as a simple residual sum of squares. For the FORCAST data, all the photometric points $6.4 \mu\text{m}$ and longer were used as well as the G111 grism data-points, excluding the region between 9.2 and $10.3 \mu\text{m}$, which is affected by telluric ozone. For the ISO data, the flux values at the FORCAST photometric points, plus the entire spectral region between 8.4 and $13.7 \mu\text{m}$ (corresponding to the G111 coverage) were used. In each set of models with fixed R_{in} , there was a value of ρ_{in} for which χ^2 was a clear minimum, which was then selected as the best-fit model. The properties of the best-fit models are given in Table 5. The reduced- χ^2 is also tabulated, but we note that the statistic was minimized to find the appropriate ρ_{in} , and not used for estimating the goodness-of-fit. Figure 3 shows the synthetic SEDs from the best-fit models overlaid on the data. For each observation we choose the model with $R_{in} = 15$ au. In each case, the four best-fit models for the different values of R_{in} are indistinguishable from each other

Table 5. Model Results

Model	R_{in} (au)	ρ_{in}^a	$T_{in}(\text{K})^b$	τ_{10}	dM/dt^c	Reduced χ^2^d
ISO	10	32.3	1080	0.12	6.4	1.8
	15	17.0	900	0.09	7.5	1.4
	20	11.3	790	0.08	8.9	1.8
	25	8.3	710	0.07	10.1	2.9
SFC4	10	14.0	950	0.05	2.8	0.9
	15	7.5	780	0.04	3.3	0.7
	20	5.3	670	0.04	4.1	0.7
	25	4.0	600	0.04	4.9	0.8
SFC5	10	11.3	1090	0.04	2.2	0.9
	15	6.0	900	0.03	2.7	0.9
	20	4.0	770	0.03	3.2	1.1
	25	3.0	680	0.03	3.7	1.6
SFC6	10	15.5	1090	0.06	3.1	0.5
	15	8.0	900	0.04	3.5	0.4
	20	5.3	780	0.04	4.1	0.4
	25	3.8	700	0.03	4.6	0.5
SFC7	10	13.0	1060	0.05	2.6	2.0
	15	7.0	860	0.04	3.1	1.5
	20	4.5	740	0.03	3.5	1.3
	25	3.3	680	0.03	4.0	1.3

^aDust density at R_{in} , in units of 10^{-20} g cm $^{-3}$ for grain bulk density of 3.0 g cm $^{-3}$.

^bDust temperature at R_{in} .

^cTotal mass loss rate in 10^{-7} M $_{\odot}$ yr $^{-1}$; assumes spherically symmetric outflow, gas-to-dust mass ratio of 263 to 1, and zero drift velocity between the dust and the gas.

^d $\chi^2/(n - 1)$ with $n = 241, 202, 195, 183, 179$ for ISO, SFC4, SFC5, SFC6, SFC7 spectra, respectively.

in the wavelength range from the NIR through $\approx 18 \mu\text{m}$, beyond which they begin to diverge slightly.

New ISO, SFC4, SFC5 Models:—For the first step in our earlier modeling we did not use these SAAO data, but instead 2MASS *JHK* values for ISO and SOFIA Cycle 5, and average values from Gromadzki et al. (2009b) for SOFIA Cycle 4. The input parameters and the model results have changed. For ISO and SFC5, the effective temperatures became 100 and 200 K lower, respectively, and the luminosity became about 17% less in both cases. For SFC4, the effective temperature became higher by 200 K, and the luminosity increased by about 27%. Consequently the best-fit

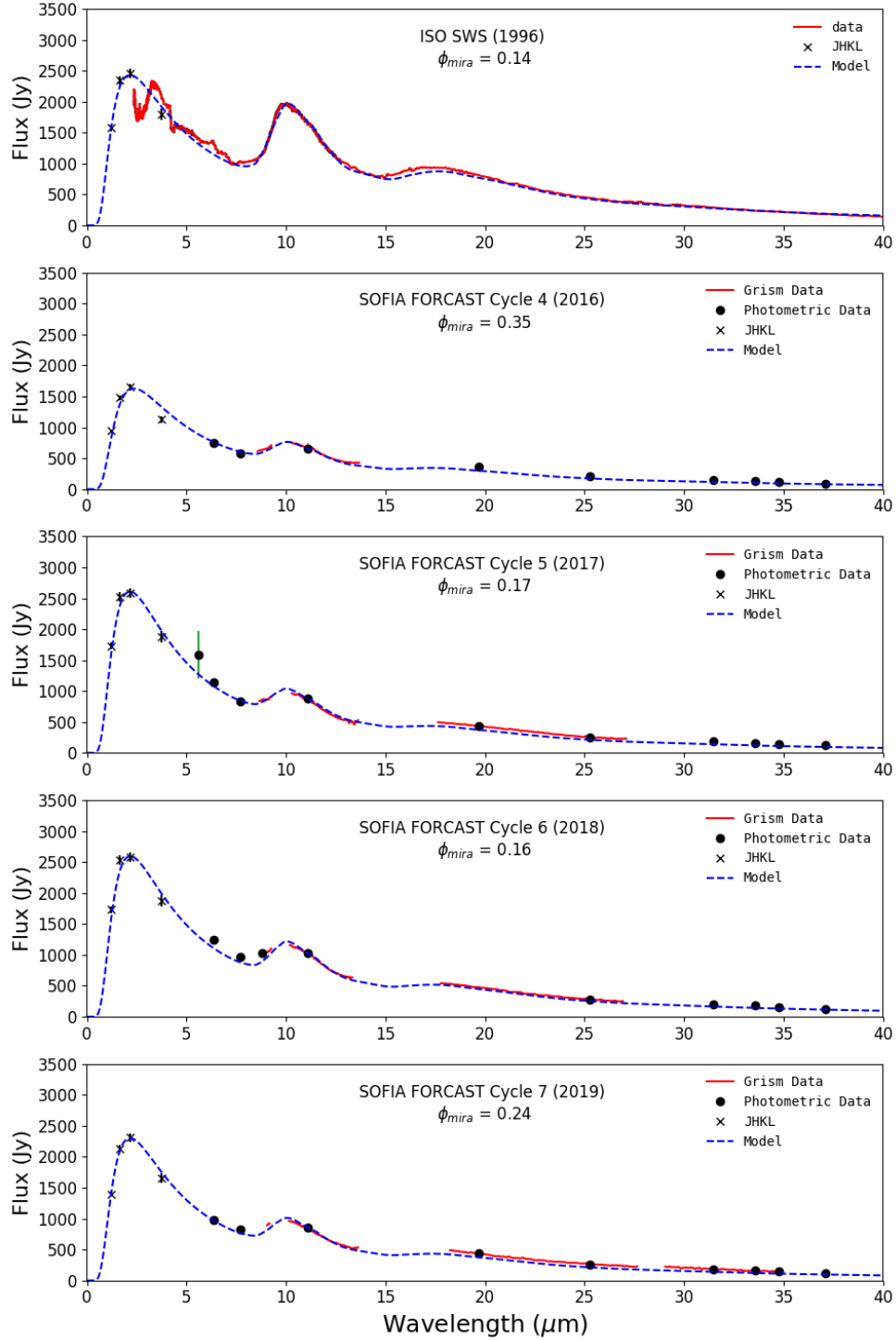


Figure 3. Plots of the $R_{in} = 15$ au best-fit models overlaid on the data. The region between 9.2 and $10.3 \mu\text{m}$, which is affected by telluric ozone, has been removed in the SOFIA FORCAST grism spectra. The JHKL values used are given in Table 3.

models' values for ρ_{in} increased for ISO and SFC5, and decreased for SFC4. The results, described in §5 of Paper 1 do not change: (i) within the one pulsation cycle that includes SFC4 and SFC5, ρ_{in} decreases between phase 0.35 and 0.17, and (ii)

there is a substantial decrease in ρ_{in} between the ISO observations and the SOFIA observations. The first result is discussed in greater detail in §5, below.

The dust temperatures in each radial zone are determined by RADMC-3D. The values predicted at the inner radius, T_{in} , represent the dust condensation temperatures, and are listed in Table 5. In all the models, $T_{dust}(r)$ decreases approximately as $r^{-0.5}$. The values of T_{in} for the best-fit models, 600–1090 K, are consistent with the range of temperatures at which silicates are able to form in circumstellar shells (e.g. Tielens 1990; Gobrecht et al. 2016). These values are also consistent with dust temperatures obtained for R Aqr in various earlier studies. (Papoular & Pégourié 1983; Anand Rao & Pottasch 1986; Danchi et al. 1994; Le Sidaner & Le Bertre 1996; Jurkic, & Kotnik-Karuza 2018).

RADMC-3D calculates the dust opacity, which depends on the optical constants, the grain bulk density, and the grain size distribution. For all our models these parameters remain the same and yield $\kappa_{10} = 2388.3 \text{ cm}^2 \text{ g}^{-1}$. The optical depths at $10 \mu\text{m}$ through the dust shell were obtained by integrating $\kappa_{10}\rho_{dust}(r)$ between R_{in} and R_{out} . The results (Table 5) are consistent with those obtained for R Aqr in earlier studies (Papoular & Pégourié 1983; Le Sidaner & Le Bertre 1996), as well as those obtained for the low mass-loss rate AGBs by Suh (2004). These low optical depths are also consistent with the silicate feature being seen in emission.

The models predict ρ_{in} in the range $(3.25\text{--}32.25)\times 10^{-20} \text{ g cm}^{-3}$. Assuming a steady wind speed of 16.7 km s^{-1} (Mayer et al. 2013), and a gas-to-dust mass ratio of 263, valid for silicates (Danchi et al. 1994), the total predicted mass loss rates range from 2.2×10^{-7} to $1.0 \times 10^{-6} \text{ M}_{\odot} \text{ yr}^{-1}$ (Table 5). These values are slightly higher than the recent estimate by Ramstedt et al. (2018) based on the CO J=3→2 line emission, but much lower than the earlier estimate of Bujarrabal et al. (2010) based on the CO J=2→1 and J=1→0 lines. Our original estimate of ρ_{in} was based on values of the mass loss rate and velocity in Danchi et al. (1994), and therefore as expected our model predictions are consistent with their results.

5. DISCUSSION

In Paper 1 we analyzed the variability of the dust emission within a pulsation cycle by examining the SOFIA Cycle 4 ($\phi_{Mira}=0.35$) and Cycle 5 ($\phi_{Mira}=0.17$) data, using spherically symmetric radiative transfer models. The overall qualitative results presented there are unchanged, but our new models require a revision of the parameter values. The effective temperature of the AGB star increases from 2200 to 2400 K between Cycle 4 and Cycle 5 observations, and the stellar radius increases from 2.30 to 2.55 au, which implies a factor 1.7 increase in the luminosity (Table 4). This is a smaller contrast than found earlier, where the luminosity increased by a factor 2.6 between the two epochs. Consequently, the implied differences in the dust density at the inner radius are also smaller than found previously.

Table 5 shows several best-fit models for each observation, each for a different value of R_{in} . There is a degeneracy induced by these parameters, which cannot be resolved within our model framework. For instance, if R_{in} is assumed to be the same over a pulsation period, then ρ_{in} is about 1.2 to 1.3 times higher at the time of Cycle 4 compared to Cycle 5 observations, and the dust condensation temperature is lower by about 100 K. If, instead, T_{in} is assumed to be the same, then the contrast in ρ_{in} is larger. As a specific case, we consider the SFC4, $R_{in}=15$ au and SFC5, $R_{in}=20$ au models. T_{in} is about the same (770 K) for both models, and the ratio of ρ_{in} is about 1.9 between SFC4 and SFC5. The models allow for ρ_{in} to be constant over a pulsation cycle, which would require that the dust condenses further away from the AGB star near minimum than near maximum.

The Cycle 6 observations were obtained almost exactly one pulsation period after the Cycle 5 observations, and show a significant increase in the mid-IR fluxes. The FORCAST fluxes are higher by 5–10% over most of the bandpass, and about 16% higher at $11.1 \mu\text{m}$, which samples the silicate emission feature. The Cycle 7 observations were obtained one pulsation cycle after Cycle 6, and at a slightly later Mira-phase. Between Cycles 6 and 7, the $11.1 \mu\text{m}$ flux has fallen by about 17%, and the fluxes at longer wavelengths by about 10%, bringing them to about the same level as in Cycle 5, and well above the fluxes in Cycle 4 (Fig. 2).

The first stage of the model-fitting used the same $JHKL$ values for both Cycles 5, and 6, and used the $6.6 \mu\text{m}$ and $7.4 \mu\text{m}$ fluxes in determining the AGB star parameters, which were found to be the same for both epochs, yielding $T_{eff} = 2400$ K and $L = 9000 L_{\odot}$ (Table 4). The best-fit models predict that for a given value of R_{in} , the dust density at the inner radius is higher by about 30% for Cycle 6 than for Cycle 5. The models for Cycle 7 yield the same T_{eff} for the AGB star as for Cycles 5 and 6, and a slightly smaller radius, implying a 12% drop in the luminosity (Table 4). The models predict that for a given R_{in} the dust density, ρ_{in} , for Cycle 7 is about 0.86 the value for Cycle 6. The degeneracies described above when comparing Cycle 4 and Cycle 5 models, apply here as well. The models do not rule out the case, for instance, that R_{in} was larger during the Cycle 6 observations than during Cycle 7, and the dust density lower.

5.1. Changes in the Dust Emission with Orbital Phase

The mid-IR flux decreased between the time of the ISO observations, which took place near apastron, and the SOFIA Cycle 5 observations just before the onset of the eclipse. By Cycle 6, the flux has started increasing again. In Paper 1 we suggested that the dust production rate in the AGB star wind reaches a peak near apastron, when the WD is beyond the dust condensation radius, and drops as the separation between the two stars decreases and the hot WD inhibits dust formation.

Within the generally accepted scenario that R Aqr is now approaching periastron and the WD is moving between us and the AGB star, the increase in the mid-IR

flux in the Cycle 6 and 7 SOFIA observations is readily explained in a qualitative way. It is due to both the enhancement of the accretion flow rate, and the orbital geometry which makes this flow and the disk around the WD visible to us. And, as first suggested by Willson et al. (1981), the intervening material is responsible for the accompanying decrease in visual brightness. A persistent dusty disk in the system also explains the presence of micron size grains, as we noted in Paper 1.

Our models suggest that the above scenario is plausible, but are not sufficient to demonstrate it quantitatively. There are two basic limitations, the first of which is that our models assume spherically symmetric dust distributions, while the real distribution is likely to be more disk-like in the regions closest to the stars, similar to what is seen in gas tracers (Ramstedt et al. 2018; Bujarrabal et al. 2018). The second, even more fundamental limitation is one hinted at above, that both the dust production rate and the accretion rate are being modulated on orbital time-scales. The dynamics of the flow needs to be modeled to obtain the dust distribution at different orbital phases, and the dust production in the AGB wind in the presence of a hot WD needs to be modeled to constrain the results of the radiative transfer calculations.

5.2. Variation with Mira-Phase

The sequence of FORCAST observations were obtained over the course of four successive pulsation cycles of R Aqr. Although the onset of the eclipse midway through the sequence complicates the issue, we can usefully examine the dependence of various parameters on the Mira-phase of the system by using the fortuitous circumstance that the phase was almost exactly the same for Cycles 5 and 6, and assuming that we can scale Cycle 4 values to Cycle 5, and Cycle 7 values to Cycle 6. We note that the AGB star parameters were determined based on out-of-eclipse *JHKL* values and therefore are consistent with the above assumption.

The variation of the $11.1\ \mu\text{m}$ flux (an observed tracer of the strength of the silicate emission feature), the AGB star luminosity (an input to the model), and the dust density at the inner radius (the key model prediction) with Mira-phase are shown in Fig. 4. These values have been normalized to 1.0 at $\phi_{Mira} = 0.165$ in the plots, which is the average of the Cycle 5 and Cycle 6 phases. The change between phases 0.16 and 0.24 is modest, with the AGB luminosity, dust density, and the $11.1\ \mu\text{m}$ flux all decreasing in lock-step. Then, by phase 0.35 the AGB luminosity has fallen to about 65% of its value at phase 0.24. This trend in luminosity is consistent with the early finding that the luminosity maximum for long-period variables is reached at a pulsation phase of about 0.14 (Pettit & Nicholson 1933), and confirmed more recently by Smith et al. (2006). Along with the decrease in the luminosity, the dust density has increased by over 30%, between these phases, and the overall effect is a slight decrease in the $11.1\ \mu\text{m}$ flux.

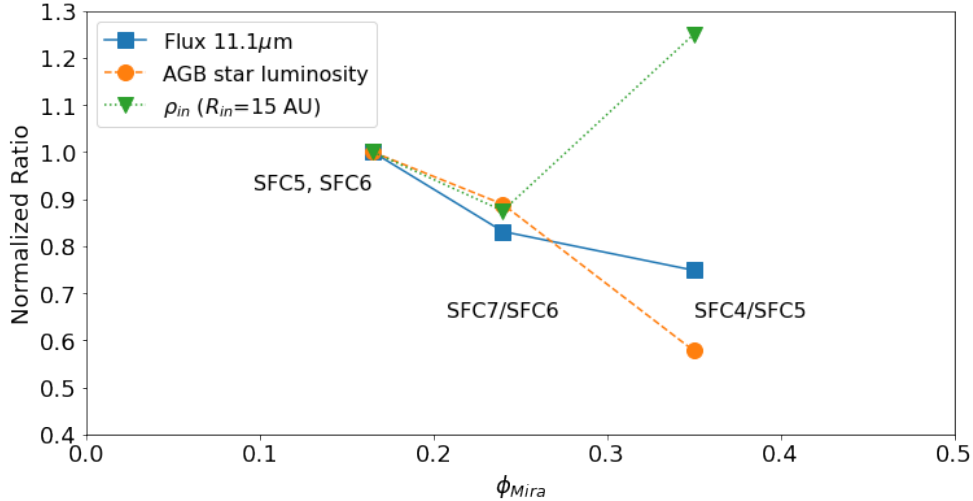


Figure 4. The observed 11.1 μm flux, the model input AGB luminosity, and the model predicted dust density at the inner radius (for $R_{in} = 15$ au models) plotted against the Mira-phase. These quantities are normalized to 1.0 at phase 0.165, and the ratios are based on values from Tables 2, 4 and 5, respectively.

Our results provide further evidence of one of the conclusions presented in Paper 1, that we do not need to invoke any change in the optical properties of the dust at different Mira phases. Rather, we find that the variations in the AGB star temperature and luminosity are sufficient to explain the changes in the silicate emission over a pulsation cycle.

6. CONCLUDING REMARKS

We have presented new SOFIA/FORCAST observations of R Aqr, which were obtained after the onset of the eclipse of the AGB star by its WD companion and the accretion flow. The drop in visual magnitude is accompanied by an increase in the mid-IR flux, and in particular the strength of the silicate emission feature. Radiative transfer models indicate that the underlying stellar spectrum heating the dust is relatively unaffected by the eclipse, and the increase in the mid-IR flux is due to higher dust densities in the outflow.

The structure of the outflow and accretion is expected to change significantly over the course of a binary orbit. The changing separation between the WD and the AGB modulates the flow structure, which in turn influences the dust production efficiency. The exploration of non-spherical dust distributions based on realistic accretion models is the topic of an ongoing study, and will be presented in a future publication. Continued monitoring of R Aqr in the mid-IR will be crucial for understanding how the dust outflow and accretion are modulated by the binary orbit.

ACKNOWLEDGMENTS

We thank the SOFIA SMO staff for their contribution towards obtaining and calibrating the data for the community. This work was supported in part by SOFIA GO grants SOF 06-0005 and SOF 07-0097 to the Space Science Institute. PAW acknowledges a research grant from the South African National Research Foundation. We are grateful to Fred Marang and Francois Van Wyk who made most of the previously unpublished *JHKL* observations.

Facilities: SOFIA, ISO, AAVSO

APPENDIX

A. NEAR-INFRARED PHOTOMETRY

Table A1. Infrared Photometry

JD-2440000	<i>J</i>	<i>H</i>	<i>K</i>	<i>L</i>
days	(mag)			
2592 ^a	2.08	0.79	-0.07	-1.17
2620	2.13	0.87	-0.02	-1.17
2646	2.14	0.87	-0.04	-1.24
2681	2.13	0.88	-0.04	-1.33
2704	2.23	0.95	0.01	-1.34
2737	2.13	0.86	-0.10	-1.47
2940	2.75	1.43	0.34	-1.03
2971	3.17	1.76	0.64	-0.80
2995	3.48	2.01	0.86	-0.57
3050	3.19	1.79	0.62	-0.97
3079	3.19	1.86	0.59	-0.98
3109	3.19	1.83	0.60	-1.01
3136	2.85	1.51	0.26	-1.29
3326.68	2.33	1.05	0.13	-1.13
3347.59	2.51	1.04	0.15	-0.99
3387.54	2.62	1.23	0.34	-0.83
3452.32	2.36	1.08	0.18	-1.03
4448.53	0.60	-0.56	-1.13	-1.92
4579.30	0.85	-0.22	-0.83	-1.68
4582.32	0.79	-0.25	-0.86	-1.69
4616.27	0.63	-0.37	-0.96	-1.80
4769.67	0.17	-0.86	-1.36	-2.28

Table A1 *continued on next page*

Table A1 (*continued*)

JD-2440000	<i>J</i>	<i>H</i>	<i>K</i>	<i>L</i>
days	(mag)			
4772.62	0.19	-0.82	-1.35	-2.25
4775.61	0.28	-0.79	-1.33	-2.19
4800.59	0.33	-0.74		-2.12
4815.58	0.42	-0.52	-1.01	-2.05
4819.57	0.44	-0.61	-1.18	-2.01
4852.44	0.78	-0.32	-0.91	-1.73
4901.34	1.15	0.03	-0.60	-1.45
4904.31	1.15	0.04	-0.60	-1.46
4907.36	1.25	0.07	-0.63	-1.43
4912.32	1.16			-1.46
4914.28	1.20	0.11	-0.48	-1.35
4915.39	1.18			-1.48
4918.33	1.23	0.07	-0.57	-1.43
4947.28	1.06	-0.02	-0.70	-1.56
4955.30	1.08	0.02	-0.61	-1.57
4958.29	1.03	-0.02	-0.64	-1.51
4960.28	0.87	-0.14	-0.78	-1.66
5157.64	0.21	-0.82	-1.35	-2.16
5181.54	0.26	-0.78	-1.33	-2.08
5193.52	0.34	-0.72	-1.28	-2.01
5215.49	0.49	-0.57	-1.12	-1.94
5251.36	0.74	-0.35	-0.92	-1.70
5280.31	0.88	-0.21	-0.78	-1.56
5543.53	0.00	-1.02	-1.56	-2.35
5544.58	0.02	-0.99	-1.50	-2.35
5545.52	0.02	-1.02	-1.55	-2.36
5546.55	0.05	-0.95	-1.47	-2.27
5548.56	0.01	-0.99	-1.49	-2.32
5567.42	0.03	-0.98	-1.56	-2.26
5571.52	0.06	-0.96	-1.48	-2.30
5595.42	0.24	-0.73	-1.22	-2.11
5602.49	0.26	-0.74	-1.31	-2.08
5612.38	0.32	-0.70	-1.26	-2.03
5613.46	0.39	-0.62	-1.19	-1.98
5615.41	0.42	-0.63	-1.20	-1.97
5626.34	0.54	-0.50	-1.07	-1.93
5637.43	0.64	-0.39	-0.97	-1.86
5649.32	0.79	-0.28	-0.87	-1.77

Table A1 *continued on next page*

Table A1 (*continued*)

JD-2440000	<i>J</i>	<i>H</i>	<i>K</i>	<i>L</i>
days	(mag)			
5681.31	1.10	0.02	-0.65	-1.57
5688.29	1.16	0.11	-0.59	-1.52
5701.26	1.23	0.14	-0.52	-1.45
5713.26	1.25	0.17	-0.53	-1.48
5873.68	0.32	-0.61	-1.17	-2.18
5892.65	0.28	-0.70	-1.24	-2.11
5896.63	0.25	-0.70	-1.24	-2.15
5920.58	0.16	-0.82	-1.34	-2.20
5958.43	0.12	-0.89	-1.41	
6023.31	0.54	-0.46	-1.03	-1.81
6031.31	0.63	-0.38	-0.96	-1.80
6070.30	1.05	-0.01	-0.65	-1.50
6075.29	1.07	0.03	-0.62	-1.44
6222.66	0.68	-0.21		-1.81
6303.49	0.08	-0.95	-1.44	-2.22
6351.39				-2.23
6391.30	0.18	-0.87	-1.40	-2.04
6596.67	0.73	-0.23	-0.80	-1.67
6638.60	0.34	-0.58	-1.09	-1.96
6658.60	0.18	-0.76	-1.27	-2.07
6692.46	0.02	-0.94	-1.43	-2.16
6712.40	-0.02	-1.01	-1.48	-2.21
6747.40	0.04	-0.97	-1.46	-2.15
6753.32	0.08	-0.94	-1.43	-2.10
6780.34	0.22	-0.79	-1.31	-1.94
6792.29	0.32	-0.71	-1.21	-1.95
7014.57	0.42	-0.48	-1.00	-1.80
7056.48	0.10	-0.84	-1.32	-2.08
7113.39	-0.09	-1.07	-1.55	-2.21
7144.28	-0.05	-1.05	-1.52	-2.18
7367.60	0.77	-0.25	-0.81	-1.56
7376.58	0.81	-0.20	-0.79	-1.56
7393.51	0.79	-0.18	-0.75	-1.56
7394.55	0.78	-0.20	-0.76	-1.59
7447.34	0.22	-0.70	-1.18	-1.96
7685.69	1.06	-0.05	-0.68	-1.39
7732.68	0.77	-0.23	-0.80	-1.51
7745.57	0.75	-0.23	-0.80	-1.62

Table A1 *continued on next page*

Table A1 (*continued*)

JD-2440000	<i>J</i>	<i>H</i>	<i>K</i>	<i>L</i>
days	(mag)			
7759.53	0.79	-0.21	-0.78	-1.60
7779.52	0.80	-0.18	-0.77	-1.60
7821.43	0.44	-0.52	-1.03	-1.85
7840.27	0.24	-0.69	-1.18	-1.97
8073.63	1.05	-0.05	-0.68	-1.43
8086.70	1.02	-0.06	-0.68	-1.48
8129.56	0.80	-0.17	-0.78	-1.69
8165.48	0.72	-0.23	-0.79	-1.63
8213.32	0.39	-0.54	-1.07	-1.90
8224.37	0.34	-0.63	-1.14	-1.97
9146.69				-1.81
9212.63	0.86	-0.25	-0.84	-1.48
9497.67	0.13	-0.89	-1.39	-2.03
9581.59	0.91	-0.17	-0.77	-1.44
9614.55	0.95	-0.13	-0.71	-1.41
9637.27	0.82	-0.20	-0.80	-1.48

^ano exact times available for the first 13 observations

REFERENCES

- Anandrao, B. G., & Pottasch, S. R. 1986, *A&A*, 262, 167
- Belczyński, K., Mikołajewska, J., Munari, U., et al. 2000, *A&AS*, 146, 407
- Bujarrabal, V., Mikołajewska, J., Alcolea, J., et al. 2010, *A&A*, 516, A19
- Bujarrabal, V., Alcolea, J., Mikołajewska, J., Castro-Carrizo, A., & Ramstedt, S. 2018, *A&A*, 616, L3
- Burgarella, D., Vogel, M., & Paresce, F. 1992, *A&A*, 262, 83
- Carpenter, J. M. 2001, *AJ*, 121, 2851
- Carter, B. S. 1990, *MNRAS*, 242, 1
- Catchpole, R. M., Robertson, B. S. C., Lloyd Evan, T. H. H., et al. 1979, *South African Astronomical Observatory Circular*, 1
- Danchi, W. C., Bester, M., Degiacomi, C. G., Greenhill, L. J., & Townes, C. H. 1994, *ApJ*, 107, 1469
- Dullemond, C. P., Juhasz, A., Pohl, A., et al. 2012, *Astrophysics Source Code Library*
- Forrest, W. J., McCarthy, J. F., & Houck, J. R. 1979, *ApJ*, 233, 611
- Gobrecht, D., Cherchneff, I., Sarangi, A., Plane, J. M. C., & Bromley, S. T. 2016, *A&A*, 585, A6
- Gromadzki, M., & Mikołajewska, J. 2009, *A&A*, 495, 931
- Gromadzki, M., Mikołajewska, J., Whitelock, P., Marang, F. 2009, *AcA*, 59, 169
- Herter, T. L., Vacca, W. D., Adams, J. D., et al. 2013, *PASP*, 125, 1393
- Jurkic, T., & Kotnik-Karuza, D. 2018, *Astronomy Letters*, 44, 265
- Kaler, J. B. 1981, *ApJ*, 245, 568
- Kraemer, K. E., Sloan, G. C., Price, S. D., & Walker, H. J. 2002, *ApJS*, 140, 389

- Le Sidaner, P. & Le Bertre, T. 1996, *A&A*, 314, 896
- Liimets, T., Corradi, R. L. M., Jones, D., et al. 2018, *A&A*, 612, A118.
- Mathis, J. S., Rumpl, W., & Nordsieck, K. H. 1977, *ApJ*, 217, 425
- Mayer, A., Jorissen, A., Kerschbaum, F., Ottensamer, R., et al. 2013, *A&A*, 549, A69
- Meier, S. R., & Kafatos, M. 1995, *ApJ*, 451, 359
- Melnikov, S., Stute, M., & Eislöffel, J. 2018, *A&A*, 612, A77
- Merrill, K. M., & Stein, W. A. 1976, *PASP*, 88, 285
- Min, C., Matsumoto, N., Kim, M. K., et al. 2014, *PASJ*, 66, 38
- Omelian, E. B., Sankrit, R., Helton, L. A., et al. 2020, *ApJ*, 898, 31. (Paper 1)
- Ossenkopf, V., Henning, T., & Mathis, J. S. 1992, *A&A*, 261, 567
- Papoular, R. & Pégourié, B. 1983, *A&A*, 128, 335
- Pettit, E. & Nicholson, S. B. 1933, *ApJ*, 78, 320
- Ramstedt, S., Mohamed, S., Olander, T., et al. 2018, *A&A*, 616, A61
- Smith, B. J., Price, S. D., & Moffett, A. J. 2006, *AJ*, 131, 612
- Solf, J., & Ulrich, H. 1985, *A&A*, 148, 274
- Speck, A. K., Barlow, M. J., Sylvester, R. J., et al. 2000, *Astronomy and Astrophysics Supplement Series*, 146, 437
- Suh, K.-W. 2004, *ApJ*, 615, 485
- Tielens, A. G. G. M. 1990, *From Miras to Planetary Nebulae: Which Path for Stellar Evolution?*, 186
- van Belle, G. T., Dyck, H. M., Benson, J. A., et al. 1996, *AJ*, 112, 2147
- Whitelock, P. A., Feast, M. W., Catchpole, R. M., et al. 1983, *MNRAS*, 203, 351
- Whitelock, P. A. 1987, *PASP*, 99, 573
- Willson, L. A., Garnavich, P., & Mattei, J. A. 1981, *Information Bulletin on Variable Stars*, No. 1961
- Wittkowski, M., Chiavassa, A., Freytag, B., et al. 2016, *A&A*, 587, A12
- Wolf, N. J. 1973, *Interstellar Dust and Related Topics*, 52, 485
- Young, E. T., Becklin, E. E., Marcum, P. M., et al. 2012, *ApJL*, 749, L17